

WHAT DETERMINES THE INCIDENCE AND EXTENT OF MG II ABSORBING GAS AROUND GALAXIES?

HSIAO-WEN CHEN¹, VIVIENNE WILD², JEREMY L. TINKER³, JEAN-RENÉ GAUTHIER¹, JENNIFER E. HELSBY¹, STEPHEN A. SHECTMAN⁴, & IAN B. THOMPSON⁴

Accepted for Publication in the Astrophysical Journal Letters

ABSTRACT

We study the connections between on-going star formation, galaxy mass, and extended halo gas, in order to distinguish between starburst-driven outflows and infalling clouds that produce the majority of observed Mg II absorbers at large galactic radii ($\gtrsim 10 h^{-1}$ kpc) and to gain insights into halo gas contents around galaxies. We present new measurements of total stellar mass (M_{star}), H α emission line strength ($\text{EW}(\text{H}\alpha)$), and specific star formation rate (sSFR) for the 94 galaxies published in H.-W. Chen et al. (2010). We find that the extent of Mg II absorbing gas, $R_{\text{Mg II}}$, scales with M_{star} and sSFR, following $R_{\text{Mg II}} \propto M_{\text{star}}^{0.28} \times \text{sSFR}^{0.11}$. The strong dependence of $R_{\text{Mg II}}$ on M_{star} is most naturally explained, if more massive galaxies possess more extended halos of cool gas and the observed Mg II absorbers arise in infalling clouds which will subsequently fuel star formation in the galaxies. The additional scaling relation of $R_{\text{Mg II}}$ with sSFR can be understood either as accounting for extra gas supplies due to starburst outflows or as correcting for suppressed cool gas content in high-mass halos. The latter is motivated by the well-known sSFR– M_{star} inverse correlation in field galaxies. Our analysis shows that a joint study of galaxies and Mg II absorbers along common sightlines provides an empirical characterization of halo gaseous radius versus halo mass. A comparison study of $R_{\text{Mg II}}$ around red- and blue-sequence galaxies may provide the first empirical constraint for resolving the physical origin of the observed sSFR– M_{star} relation in galaxies.

Subject headings: cosmology: observations—galaxies:halos—intergalactic medium—quasars:absorption lines

1. INTRODUCTION

The Mg II $\lambda\lambda 2796, 2803$ absorption doublets are commonly seen in photo-ionized gas of temperature $T \sim 10^4$ K (Bergeron & Stasinska 1986; Charlton et al. 2003) and in high-column density clouds of neutral hydrogen column density $N(\text{HI}) \approx 10^{18} - 10^{22} \text{ cm}^{-2}$ (Rao et al. 2006). While Mg II absorbers are observed to arise in outflowing gas along the lines of sight directly into star-forming regions (e.g. Weiner et al. 2009; Martin & Bouché 2009; Rubin et al. 2010), it is unclear whether the absorbers found at projected distances beyond $\rho \sim 10 h^{-1}$ kpc from star-forming regions are primarily due to outflows, infalling clouds, or a combination thereof (c.f. Bouché et al. 2007; Ménard et al. 2010; Chelouche & Bowen 2010; Tinker & Chen 2008; Chen & Tinker 2008; Kacprzak et al. 2010; Gauthier et al. 2010).

The large wavelengths of the doublet transitions, together with recently available UV sensitive spectrographs on the ground, allow us to examine in detail the physical connections between the cool gas probed by Mg II absorption features and galaxies routinely found at redshifts as low as $z \sim 0.1$ (e.g. Barton & Cooke 2009; H.-W. Chen et al. 2010). Using a sample of 94 random galaxies at $z = 0.1 - 0.5$ and $\rho \lesssim 120 h^{-1}$ kpc from the line of sight of a background QSO, H.-W. Chen et al. (2010; hereafter C10) examined how the incidence and extent of Mg II absorbers depends on galaxy properties. They confirmed that the rest-frame absorption equivalent widths of

Mg II absorbers, $W_r(2796)$, decline with increasing projected distances from the galaxies, and found that the extent of Mg II absorbing gas, $R_{\text{Mg II}}$, depends sensitively on the galaxy B -band luminosity following $R_{\text{Mg II}} = 75 \times (L_B/L_{B*})^{(0.35 \pm 0.03)} h^{-1}$ kpc, but not on the rest-frame $B_{AB} - R_{AB}$ color or redshift. The lack of correlation between $W_r(2796)$ and $B_{AB} - R_{AB}$ color suggests a lack of physical connection between the observed Mg II absorbing gas and the recent star formation history of the galaxies. It is therefore challenging to attribute the majority of Mg II absorbers found at large galactic radii ($\gtrsim 10 h^{-1}$ kpc) to starburst-driven outflows.

However, the strong scaling relation between $R_{\text{Mg II}}$ and galaxy B -band luminosity, while interesting, is difficult to interpret. Although it has been shown that L_B scales with halo mass M_h (e.g. X. Yang et al. 2005; Tinker et al. 2007; Z. Zheng et al. 2007), L_B is also found to correlate with [O II] luminosity despite showing a large scatter (G. Zhu et al. 2009). It is not clear whether L_B is a better tracer of halo mass or on-going star formation. Here we supplement the galaxy data published in C10 with new measurements of total stellar mass M_{star} (a more robust tracer of dark matter halo mass, e.g. More et al. 2010), H α emission line strength $\text{EW}(\text{H}\alpha)$, and specific star formation rate $\text{sSFR} \equiv \text{SFR}/M_{\text{star}}$ of the galaxies. These empirical quantities allow us to investigate possible correlations between on-going star formation, galaxy mass, and absorber strength, and to identify whether on-going star formation rate or halo mass is the dominant factor in determining the incidence and extent of Mg II absorbing gas at large galactic radii. We adopt a Λ cosmology, $\Omega_M = 0.3$ and $\Omega_\Lambda = 0.7$, with a dimensionless Hubble constant $h = H_0/(100 \text{ km s}^{-1} \text{ Mpc}^{-1})$ throughout the paper.

2. STELLAR POPULATION SYNTHESIS ANALYSIS

In order to derive M_{star} and sSFR for each galaxy in our sample, we follow the maximum likelihood method now rou-

¹ Dept. of Astronomy & Astrophysics and Kavli Institute for Cosmological Physics, University of Chicago, Chicago, IL, 60637, U.S.A. hchen@oddjob.uchicago.edu

² Institut d'Astrophysique de Paris, CNRS, Université Pierre & Marie Curie, UMR 7095, 98bis bd Arago, 75014 Paris, France

³ Berkeley Center for Cosmological Physics, University of California-Berkeley

⁴ The Observatories of Carnegie Institution for Science, 813 Santa Barbara St., Pasadena, CA 91101

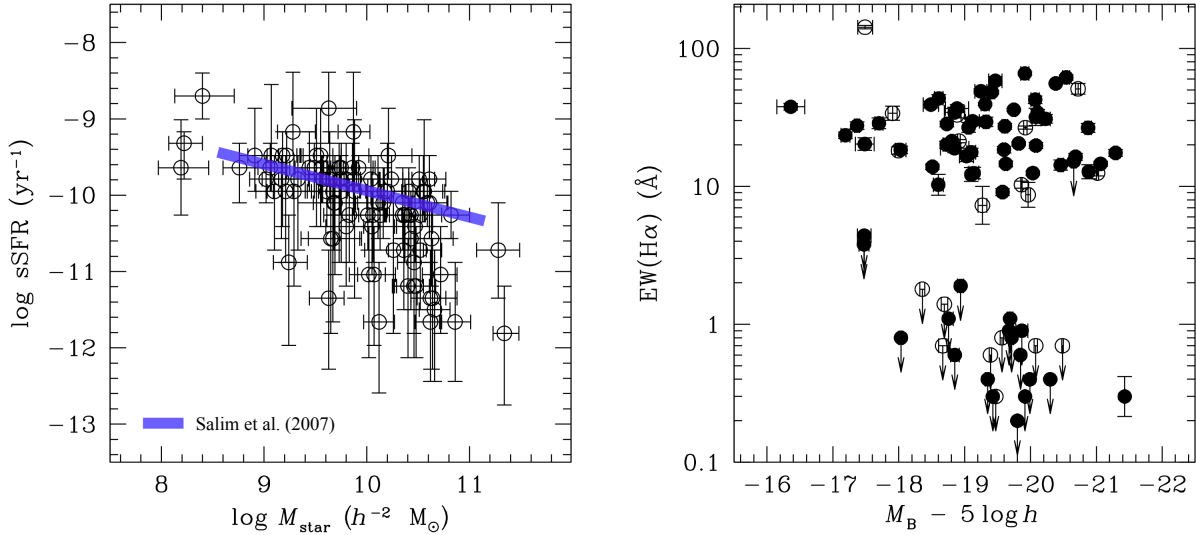


FIG. 1.— General properties of the galaxies in C10. *Left*: Comparison of the specific star formation rate (sSFR) and total stellar mass estimated from our stellar population synthesis analysis. The errorbars represent the 68% confidence interval of the PDF around the best-fit values. The plot shows that while the uncertainties of the sSFR are large, our galaxies occupy a parameter space consistent with what is seen in random field galaxies, including the blue-sequence galaxies marked by the solid line ($\log \text{sSFR} = -0.35(\log M_{\text{star}} + 2 \log h - 9.69) - 9.83$) from Salim et al. (2007) and red galaxies underneath it. *Right*: Comparison of H α emission line strength and rest-frame B-band absolute magnitude, M_B . Arrows represent 2- σ upper limits of EW(H α) for galaxies with no H α detected. The distribution of data points are also similar to what is seen in nearby galaxies (e.g. Lee et al. 2007).

tinely adopted to extract galaxy properties from wide-field survey data (Kauffmann et al. 2003; Brinchmann et al. 2004; Salim et al. 2005; Walcher et al. 2008). The basic principle is to calculate the χ^2 between a set of galaxy observables and equivalent model-galaxy predictions. The predictions are derived from a suite of stellar population synthesis models designed to cover the full range in physical properties of the observed galaxies (e.g. age, star formation history, metallicity, dust content etc.).

The benefit of this methodology over traditional methods of fitting a small number of model templates, is in the calculation of a full probability distribution function (PDF) for each physical property, which for a set of observables attempts to account for any degeneracy between derived properties. In turn, this provides a robust error estimate for each derived property. The disadvantages are that the method relies heavily upon the accuracy of stellar population synthesis models, and can be somewhat dependent on the prior distribution of physical properties assumed when creating the library of model-galaxies. Stellar population models have advanced greatly in the last decade, with the development of new empirical and theoretical stellar libraries and stellar evolutionary tracks (e.g. Bruzual 2010). Results using different model priors have also been compared and contrasted (e.g. Pozzetti et al. 2007). Overall, the consensus is that M_{star} and sSFR (which in the model is the mean SFR averaged over the last 10 Myr, divided by M_{star}) can be robustly determined, but may suffer from systematic offsets (by as much as a factor of two) between the adoption of different population synthesis models, initial-mass-functions and star formation history (SFH) priors.

The library of models used in this study is described in detail in da Cunha et al. (2008). In summary, the stellar population models are based on those described in Bruzual & Charlot (2003) revised to include a new prescription for the TP-AGB evolution of low and intermediate mass stars (Marigo & Girardi 2007). The SFH of the library of model galax-

ies is parameterized by two components (Kauffmann et al. 2003): an underlying exponentially declining SFH characterized by an age and decline timescale, and superimposed random bursts. The metallicity of the models is distributed uniformly between 0.02 and 2 times solar. The stellar continuum light is attenuated according to the two-component dust model of Charlot & Fall (2000). For each model-galaxy in our library we calculate observed-frame colors at redshifts uniformly distributed between $z = 0$ and $z = 0.5$, with a spacing of $\delta z = 0.05$.

3. GALAXY PROPERTIES

All the galaxies in our sample are observed by the SDSS (York et al. 2000) and have u, g, r, i, z photometry. To obtain accurate colors we use fixed aperture magnitudes with radii equal to the Petrosian radius⁵ in the r-band. All magnitudes are corrected for Galactic extinction. To identify the best-fit stellar population model for each observed galaxy, we calculate the χ^2 between the observed optical colors and derived values of the set of model galaxies at the appropriate redshift. We are able to constrain M_{star} and sSFR for all but three galaxies in the sample. The results are presented in Table 1. The distribution of derived M_{star} versus sSFR is shown in the left panel of Figure 1, along with the best-fit correlation of the blue-sequence galaxies from Salim et al. (2007). The errorbars represent the 68% confidence interval of the PDF around the best-fit values. We find that while the uncertainties of the sSFR are large, our galaxies occupy a parameter space consistent with what is seen in random field galaxies, including the blue-sequence marked by the solid line and the red galaxy population underneath it⁶.

⁵ <http://www.sdss.org/dr7/algorithms/photometry.html>

⁶ We note that measurements of M_{star} and sSFR remain unchanged within the errors, when we include in the model analysis available near-IR colors from the UKIDSS survey (Lawrence et al. 2007) and available EW(H α). Because these measurements are not available for all galaxies, we do not include them for consistency.

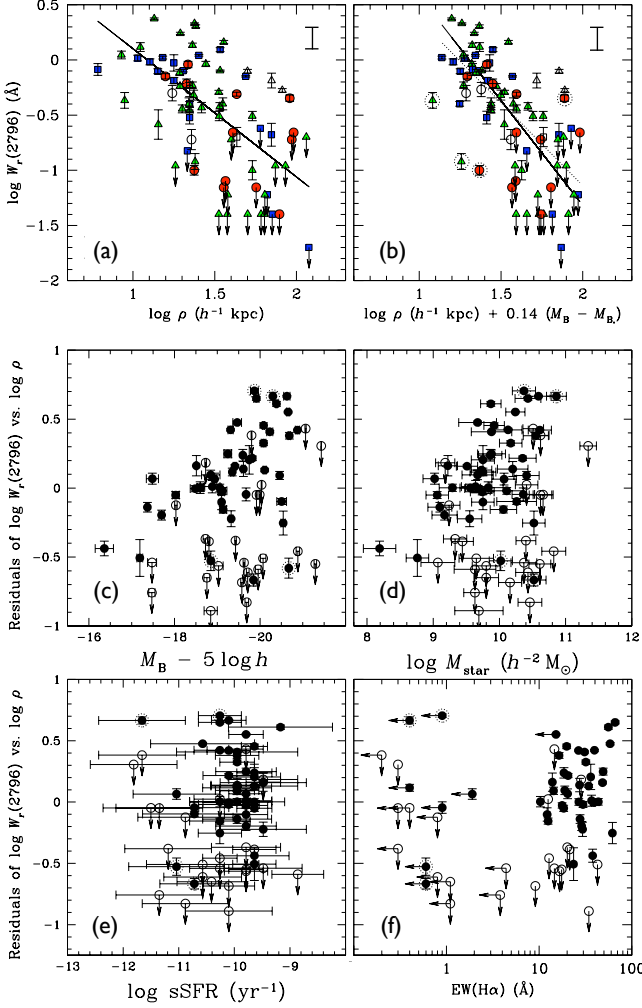


FIG. 2.— The correlation between observed Mg II absorption strength, $W_r(2796)$, and different galaxy properties. The top panels are duplicated from C10, showing the $W_r(2796)$ versus ρ anti-correlation before (panel a) and after (panel b) accounting for the scaling relation with galaxy B -band luminosity. Circles are for galaxies of rest-frame $B_{AB} - R_{AB} > 1.1$; triangles for $0.6 < B_{AB} - R_{AB} \leq 1.1$; and squares for $B_{AB} - R_{AB} < 0.6$. Arrows indicate a $2\text{-}\sigma$ upper limit of $W_r(2796)$, when Mg II absorption features are not detected. Open symbols represent galaxies with known close neighbors and are not included in the model fit. The solid and dotted lines are the best-fit models, excluding and including the outliers (points in dotted circles), respectively. Panels (c)–(f) present the residuals seen in panel (a) versus M_B , M_{star} , sSFR, and $\text{EW}(\text{H}\alpha)$. Solid points represent galaxies with detected Mg II absorbers, while open points represent those galaxies with no detections. Left arrows indicate the $2\text{-}\sigma$ upper limit of $\text{EW}(\text{H}\alpha)$ when the $\text{H}\alpha$ emission is not observed. A comparison between panels (c) through (f) suggests that the observed Mg II absorber strengths depend on galaxy B -band magnitude and total stellar mass, but do not depend on sSFR or $\text{EW}(\text{H}\alpha)$.

In addition to the broad-band photometric colors, we measure the rest-frame $\text{H}\alpha$ emission equivalent width, $\text{EW}(\text{H}\alpha)$, using available galaxy spectra from C10⁷. $\text{EW}(\text{H}\alpha)$ measures the on-going star formation rate relative to the past average (e.g. Lee et al. 2009), and provides an independent, empirical estimate of the sSFR. The measurements are presented in Column (5) of Table 1. When the $\text{H}\alpha$ emission is not observed, we place a $2\text{-}\sigma$ upper limit. The right panel of Figure 1 shows the correlation between $\text{EW}(\text{H}\alpha)$ and the rest-frame B -band

absolute magnitude, $M_B - 5 \log h$, of the galaxies, similar to what is seen in nearby galaxies (e.g. Lee et al. 2007).

4. DEPENDENCE OF $W_r(2796)$ ON GALAXY PROPERTIES

To examine the dependence of $W_r(2796)$ on galaxy properties, we first briefly review the findings of C10. The top panels of Figure 2 are duplicated from C10. Panel (a) shows that with a large scatter $W_r(2796)$ on average declines with increasing projected distance from the absorbing galaxy, ρ . Panel (b) of Figure 2 shows that, including the optimal scaling with galaxy B -band luminosity, the $W_r(2796)$ vs. ρ anti-correlation is significantly improved. Different symbols indicate different rest-frame $B_{AB} - R_{AB}$ color of the galaxies, showing qualitatively that $W_r(2796)$ does not depend sensitively on galaxy intrinsic colors (see C10 for details). Roughly 20% of the galaxies with $M_B - 5 \log h \leq -18.5$ in this sample have $B_{AB} - R_{AB}$ color consistent with elliptical or S0. No clear trend is seen between M_B and $B_{AB} - R_{AB}$.

Including new measurements of M_{star} , sSFR, and $\text{EW}(\text{H}\alpha)$, we present the residuals of the $W_r(2796)$ vs. ρ anti-correlation (panel a of Figure 2) versus M_B , M_{star} , sSFR, and $\text{EW}(\text{H}\alpha)$ in panels (c)–(f) of Figure 2, respectively. Inspecting the residuals versus different galaxy properties, we find that qualitatively the observed Mg II absorber strengths depend sensitively on M_B and M_{star} , but not on sSFR or $\text{EW}(\text{H}\alpha)$.

We also perform the likelihood analysis described in C10, in order to quantify the best-fit correlation between $W_r(2796)$ and different galaxy properties in the presence of non-detections in the Mg II features. Adopting a power-law model,

$$\log \bar{W}_r(2796) = a_0 + a_1 \log \rho + a_2 X, \quad (1)$$

we seek the best-fit coefficients, a_0 , a_1 , and a_2 that minimize the scatter in the $W_r(2796)$ versus ρ anti-correlation. We first consider M_B and M_{star} separately.

Assigning $X \equiv \log M_{\text{star}} - 10.3$, we find that the Mg II gaseous extent scales with ρ and M_{star} following $a_1 = -1.8 \pm 0.1$ and $a_2 = 0.34 \pm 0.06$ in Equation (1). For a fixed $W_r(2796)$, we find that more massive galaxies possess more extended Mg II absorbing gas. The extent of Mg II absorbing gas at fixed $W_r(2796)$, $R_{\text{Mg II}}$, is found to scale with M_{star} following $R_{\text{Mg II}} \propto M_{\text{star}}^{0.19 \pm 0.03}$. The results are presented in panel (a) of Figure 3, where we have also adopted different symbols to highlight different ranges of sSFR. The best-fit model has an associated intrinsic scatter (see C10 for definition) of $\sigma_c = 0.208$ and a r.m.s. residual between the observed and model Mg II absorber strengths of $\text{r.m.s.}(\log W_r - \log \bar{W}) = 0.269$. We find that, similar to M_B , including M_{star} indeed improves the scatter found in the $W_r(2796)$ vs. ρ anti-correlation, although the M_{star} -corrected relation exhibits a somewhat larger scatter. At the same time, the lack of a systematic trend between the residuals and sSFR suggests that sSFR has little impact on the extended Mg II absorbing gas at large galactic radii.

Assigning $X \equiv \log \text{sSFR} + 10.3$, we find that the Mg II gaseous extent scales with ρ and sSFR following $a_1 = -1.3 \pm 0.1$ and $a_2 = 0.15 \pm 0.04$ in Equation (1). The best-fit coefficients lead to $R_{\text{Mg II}} \propto \text{sSFR}^{0.12 \pm 0.03}$ at fixed $W_r(2796)$, suggesting that galaxies with higher sSFR possess more extended Mg II absorbing gas. The best-fit model has an associated intrinsic scatter of $\sigma_c = 0.219$ and a r.m.s. residual between the observed and model Mg II absorber strengths of $\text{r.m.s.}(\log W_r - \log \bar{W}) = 0.284$. Panel (b) of Figure 3 shows that the remaining scatter in the sSFR-corrected $W_r(2796)$ vs.

⁷ We measure $\text{EW}(\text{H}\alpha)$ instead of $\text{H}\alpha$ line fluxes, because the spectra have not been corrected for aperture or differential slit losses.

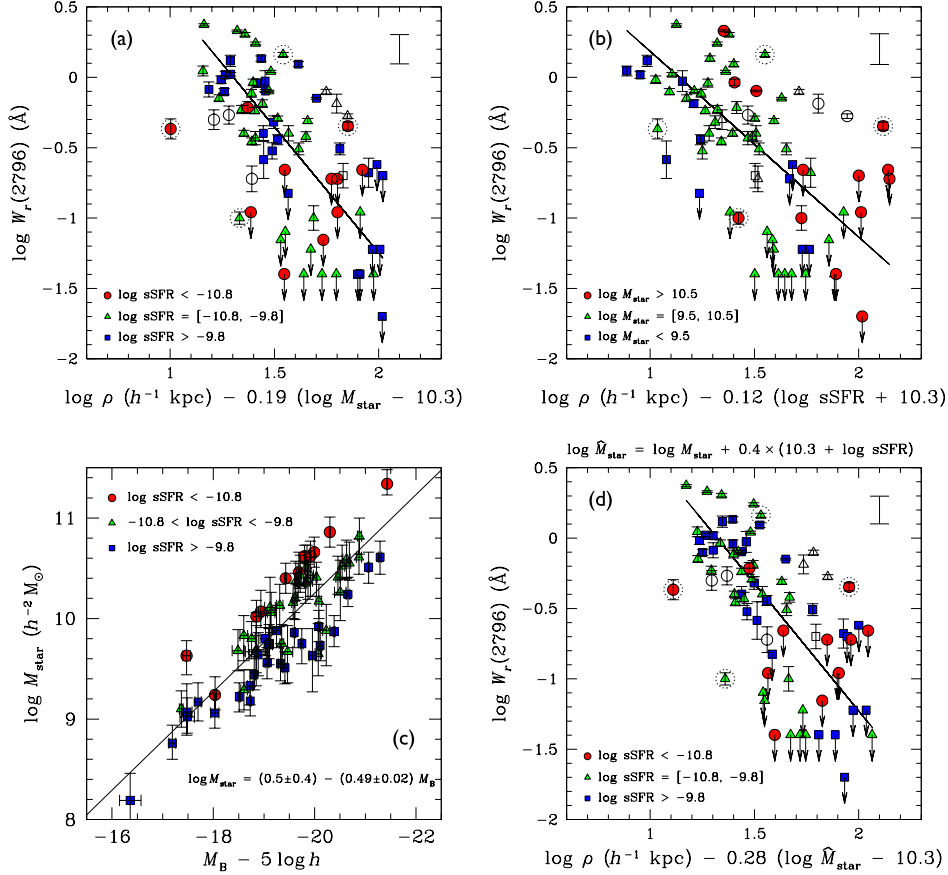


FIG. 3.— Searching for the physical properties that determine the incidence and extent of Mg II absorbing gas around galaxies. Panel (a) shows the observed $W_r(2796)$ vs. ρ anti-correlation, including an optimal scaling relation with M_{star} . Different symbols represent different ranges in the associated sSFR. Panel (b) shows the observed $W_r(2796)$ vs. ρ anti-correlation, including an optimal scaling relation with the associated sSFR. Different symbols represent different ranges in M_{star} . The same as panels (a) and (b) of Figure 1, the open symbols represent galaxies with known close neighbors and are excluded from the model fit. Panel (c) shows that while more luminous galaxies have higher stellar mass, more massive galaxies also exhibit an on-average lower sSFR (see Figure 1 and Salim et al. 2007). Panel (d) shows that including sSFR-corrected M_{star} further reduces the scatter in the observed $W_r(2796)$ vs. ρ anti-correlation.

ρ anti-correlation is large and there exists an apparent systematic trend between the residuals of the mean relation and M_{star} as indicated by different symbols in the panel.

Combining the results shown in panels (a) and (b) of Figure 3, we find that the scatter in the observed $W_r(2796)$ vs. ρ anti-correlation is driven primarily by M_{star} of the galaxies. However, the remaining scatter is still somewhat larger than what is seen after accounting for the scaling relation with galaxy B -band luminosity (panel b of Figure 2), implying that M_B is a more successful than M_{star} in determining the extent of Mg II absorbing gas.

To understand the difference, we examine the correlation between M_{star} , M_B , and sSFR in panel (c) of Figure 3. We find that while more luminous galaxies have higher stellar mass, on average more massive galaxies also exhibit lower sSFR. Applying a χ^2 analysis for estimating the best-fit M_{star} -sSFR correlation that reduces the observed scatter, we find that $\log M_{\text{star}} \propto (-0.4 \pm 0.1) \log \text{sSFR}$ for a fixed M_B . This best-fit correlation is steeper than what is seen in the blue-sequence galaxies (e.g. Salim et al. 2007), because the χ^2 analysis is based on the entire galaxy sample that includes both red- and blue-sequence galaxies (Figure 1).

Adopting sSFR-corrected M_{star} , $\log \hat{M}_{\text{star}} = \log M_{\text{star}} + 0.4(10.3 + \log \text{sSFR})$ and repeating the likelihood analysis

to seek the best-fit coefficients in Equation (1) yield $a_1 = -1.8 \pm 0.1$ and $a_2 = 0.5 \pm 0.05$, leading to

$$R_{\text{Mg II}} \propto M_{\text{star}}^{0.28 \pm 0.03} \times \text{sSFR}^{0.11 \pm 0.03}. \quad (2)$$

The results are presented in panel (d) of Figure 3. The best-fit model has an associated intrinsic scatter of $\sigma_c = 0.195$ and a r.m.s. residual between the observed and model Mg II absorber strengths of $\text{r.m.s.}(\log W_r - \log \hat{W}) = 0.241$. We find that including both M_{star} and sSFR reproduces the strong anti-correlation determined using M_B seen in panel (b) of Figure 2.

5. DISCUSSION

Our analysis shows that the extent of Mg II absorbing gas depends strongly on M_{star} and more weakly on sSFR, following $R_{\text{Mg II}} \propto M_{\text{star}}^{0.28} \times \text{sSFR}^{0.11}$. The strong dependence of $W_r(2796)$ on M_B (C10) is understood as M_B being an integrated measure of M_{star} and sSFR in galaxies. The empirical data demand a scaling relation that includes both M_{star} and sSFR, with M_{star} being a more dominant factor. A tight correlation is found between M_{star} and halo mass (e.g. More et al. 2010). The strong dependence between $R_{\text{Mg II}}$ and M_{star} is naturally explained, if Mg II absorbers arise in infalling clouds and more massive galaxies possess more extended halos of

cool gas (e.g. Mo & Miralda-Escudé 1996; Maller & Bullock 2004; Tinker & Chen 2008). Our analysis shows that a joint study of galaxies and Mg II absorbers along common sight-lines allows an empirical characterization of halo gaseous radius versus halo mass.

On the other hand, there are two possible interpretations of the additional scaling relation between $R_{\text{Mg II}}$ and sSFR. The first scenario is that Mg II absorbing gas is produced in wind-blown materials that, around galaxies of the same mass, can reach to larger distances at higher SFR. Likewise, around galaxies of the same SFR outflows can reach to larger distances in lower-mass halos. In this scenario, the gas contents of extended halos around galaxies are regulated by both accretion and outflows, however, accretion remains the dominant process.

Alternatively, we consider the inverse correlation between sSFR and M_{star} commonly seen in field galaxies over a broad redshift range that has been studied (e.g. Figure 1; Salim et al. 2007; X.-Z. Zheng et al. 2007; Y.-M. Chen et al. 2009). More massive galaxies on average exhibit lower sSFR. In particular, red galaxies show an overall much reduced rate of star formation in comparison to the blue-sequence galaxies, suggesting a suppressed gas supply around these red galaxies (e.g. Schiminovich et al. 2007). Instead of gaseous halos being enriched with starburst driven outflows, the additional scaling relation between $R_{\text{Mg II}}$ and sSFR in Equation (2) can therefore be understood as due to an increasingly suppressed cool gas supply around higher-mass galaxies. In this scenario, Mg II absorbers serve as a direct measure of gas supply around galaxies.

The physical processes that produce the bi-modality of red and blue galaxies and the tilt of the sSFR– M_{star} relation in the blue sequence remain uncertain. While it is generally understood that SFR follows the net accretion rate of cool gas (e.g. Birnboim & Dekel 2003; Kereš et al. 2005, 2009), achieving galaxy bi-modality in simulations using feedback, mergers etc. does not necessarily reproduce the time-evolution of

the sSFR– M_{star} relation for the blue sequence galaxies (e.g. Davé 2008; Bouché et al. 2010). If observations of Mg II absorbers around galaxies give a direct measure of how the cool halo gas content varies with galaxy mass, a comparison study of the Mg II gaseous extent around red- and blue-sequence galaxies may provide the first empirical constraint for resolving the physical origin of the observed sSFR– M_{star} relation in galaxies.

Finally, we note the remaining large scatter in the $W_r(2796)$ vs. ρ anti-correlation after accounting for the differences in M_{star} and sSFR. Given the range of M_B , $B_{AB} - R_{AB}$, M_{star} , and sSFR covered by the galaxy sample, it is not clear whether any single physical mechanism can explain such scatter for the entire sample. C10 attributed such scatter to Poisson noise in the number of cool clumps intercepted along a line of sight. Under a clumpy halo scenario, we can begin to constrain the size and mass of individual clumps based on known properties of Mg II absorbers.

We thank Stéphane Charlot for providing the updated spectral library, and Lynn Matthews and Michael Rauch for helpful comments on an earlier version of the paper. H.-W.C. acknowledges partial support from an NSF grant AST-0607510. VW acknowledges support from a Marie Curie Intra-European fellowship. We thank the SDSS collaboration for producing and maintaining the SDSS public data archive. Funding for the SDSS and SDSS-II was provided by the Alfred P. Sloan Foundation, the Participating Institutions, the National Science Foundation, the U.S. Department of Energy, the National Aeronautics and Space Administration, the Japanese Monbukagakusho, the Max Planck Society, and the Higher Education Funding Council for England. The SDSS was managed by the Astrophysical Research Consortium for the Participating Institutions.

REFERENCES

- Barton, E. J. & Cooke, J. 2009, *AJ*, 138, 1817
 Bergeron, J. & Stasinska, G. 1986, *A&A*, 169, 1
 Birnboim, Y. & Dekel, A. 2003, *MNRAS*, 345, 349
 Bouché, N., Murphy, M. T., Péroux, C., Davies, R., Eisenhauer, F., Förster-Schreiber, N. M., & Tacconi, L. 2007, *ApJ*, 669, L5
 Bouché, N., Dekel, A., Genzel, R. et al. 2010, *ApJ*, 718, 1001
 Brinchmann J., Charlot S., White S. D. M., Tremonti C., Kauffmann G., Heckman T., & Brinkmann J., 2004, *MNRAS*, 351, 1151
 Bruzual, A. G. & Charlot S. 2003, *MNRAS*, 344, 1000
 Bruzual, A. G. 2010, in *IAU Symposium Vol. 262*, p. 55
 Charlot S. & Fall S. M. 2000, *ApJ*, 539, 718
 Charlton, J. C., Ding, J., Zonak, S. G., Churchill, C. W., Bond, N. A., & Rigby, J. R. 2003, *ApJ*, 589, 111
 Chelouche, D. & Bowen, D. V. 2010, *arXiv:1008.2769*
 Chen, H.-W. & Tinker, J. L. 2008, *ApJ*, 687, 745
 Chen, H.-W., Helsby, J. E., Gauthier, J.-R., Shectman, S. A., Thompson, I. A., & Tinker, J. L. 2010, *ApJ*, 714, 1521 (C10)
 Chen, Y. M., Wild, V., & Kauffmann, G. et al. 2009, *MNRAS*, 393, 406
 da Cunha E., Charlot S., & Elbaz D. 2008, *MNRAS*, 388, 1595
 Davé, R. 2008, *MNRAS*, 385, 147
 Gauthier, J.-R., Chen, H.-W., & Tinker, J. L. 2010, *ApJ*, 716, 1263
 Kacprzak, G. G., Churchill, C. W., Ceverino, D., Steidel, C. C., Klypin, A., & Murphy, M. T. 2010, *ApJ*, 711, 533
 Kauffmann G., Heckman T. M., & White S. D. M., et al. 2003, *MNRAS*, 341, 33
 Kereš, D., Katz, N., Weinberg, D. H., & Davé, R. 2005, *MNRAS*, 363, 2
 Kereš, D., Katz, N., Fardel, M., Davé, R., & Weinberg, D. H. 2009, *MNRAS*, 395, 160
 Lawrence, A. et al. 2007, *MNRAS*, 379, 1599
 Lee, J. C., Kennicutt, R. C., Funes, S. J., José, G., Sakai, S., & Akiyama, S. 2007, *ApJ*, 671, L113
 ———, 2009, *ApJ*, 692, 1305
 Maller, A. H. & Bullock, J. S. 2004, *MNRAS*, 355, 694
 Marigo, P. & Girardi, L. 2007, *A&A*, 469, 239
 Martin, C. L. & Bouché, N. 2009, *ApJ*, 703, 1394
 Ménard, B., Wild, V., Nestor, D., Quider, A., & Zibetti, S. 2010, *MNRAS* submitted (*arXiv:0912.3263*)
 Mo, H. J. & Miralda-Escudé, J. 1996, *ApJ*, 469, 589
 More, S. et al. 2010, *MNRAS* submitted (*arXiv:1003.3203*)
 Pozzetti L., Bolzonella M., & Lamareille F., et al. 2007, *A&A*, 474, 443
 Rao, S. M., Turnshek, D. A., & Nestor, D. B. 2006, *ApJ*, 636, 610
 Rubin, K. H. et al. 2010, *ApJ*, 719, 1503
 Salim S. et al. 2005, *ApJ*, 619, L39
 Salim S. et al. 2007, *ApJS*, 173, 267
 Schiminovich, D. et al. 2007, *ApJS*, 173, 315
 Tinker, J. L., Norberg, P., Weinberg, D. H., & Warren, M. S. 2007, *ApJ*, 659, 877
 Tinker, J. L. & Chen, H.-W. 2008, *ApJ*, 679, 1218
 Walcher C. J., Lamareille F., & Vergani D., et al. 2008, *A&A*, 491, 713
 Weiner, B. J. et al. 2009, *ApJ*, 692, 187
 Yang, X. et al. 2005, *MNRAS*, 358, 217
 York, D. G. et al. 2000, *AJ*, 120, 1579
 Zheng, X. Z., Bell, E., & Papovich, C. et al. 2007, *ApJ*, 661, L41
 Zheng, Z., Coil, A. L., & Zehavi, I. 2007, *ApJ*, 667, 760
 Zhu, G., Moustakas, J., & Blanton, M. R. 2009, *ApJ*, 701, 86

TABLE 1
SUMMARY OF ADDITIONAL GALAXY PROPERTIES IN CHEN ET AL. (2010)^a

Galaxy ID (1)	z_{spec} (2)	$\log(M_{\text{star}}/h^2 M_{\odot})$ (3)	$\log \text{sSFR}/\text{yr}^{-1}$ (4)	EW(H α) (\AA) ^b (5)
SDSSJ003339.85-005522.36	0.2124	9.7 ± 0.2	-9.6 ± 0.8	34.2 ± 1.8
SDSSJ003407.78-085453.28	0.3617	9.6 ± 0.2	-9.8 ± 0.5	36.8 ± 2.3
SDSSJ003412.85-010019.79	0.2564	10.1 ± 0.2	-11.0 ± 0.8	< 1.9
SDSSJ003414.49-005927.49	0.1202	10.6 ± 0.1	-11.7 ± 0.8	< 0.2
SDSSJ010136.52-005016.44	0.2615	10.4 ± 0.2	-10.6 ± 0.7	< 0.8
SDSSJ010155.80-084408.74	0.1588	9.2 ± 0.2	-9.8 ± 0.5	28.7 ± 2.6
SDSSJ010351.82+003740.77	0.3515	9.7 ± 0.2	-10.0 ± 0.4	18.9 ± 1.4
SDSSJ021558.84-011131.23	0.2103	9.8 ± 0.2	-10.0 ± 0.6	< 0.4
SDSSJ022949.97-074255.88	0.3866	9.7 ± 0.3	-10.6 ± 0.9	58.3 ± 4.2
SDSSJ024127.75-004517.04	0.1765	10.5 ± 0.2	-11.2 ± 0.9	< 0.6
SDSSJ032230.27+003712.72	0.1833	10.2 ± 0.2	-9.5 ± 0.5	12.5 ± 0.6
SDSSJ032232.55+003644.68	0.2185	9.0 ± 0.2	-9.8 ± 0.3	20.3 ± 2.1
SDSSJ035241.99+001317.13	0.3671	10.4 ± 0.2	-10.3 ± 0.4	< 0.9
SDSSJ040404.51-060709.46	0.2387	9.5 ± 0.2	-9.6 ± 0.3	33.1 ± 1.7
SDSSJ075001.34+161301.92	0.1466	8.8 ± 0.2	-9.6 ± 0.4	23.5 ± 1.3
SDSSJ075450.11+185005.28	0.2856	10.5 ± 0.2	-10.9 ± 0.8	< 1.1
SDSSJ075525.13+172825.79	0.2541	10.4 ± 0.2	-10.1 ± 0.5	20.5 ± 0.6
SDSSJ080005.11+184933.31	0.2544	9.6 ± 0.2	-9.5 ± 0.8	29.4 ± 2.3
SDSSJ082340.56+074751.07	0.1864	10.4 ± 0.2	-10.7 ± 0.6	< 0.9
SDSSJ084120.59+012628.85	0.4091	10.5 ± 0.2	-10.3 ± 0.4	61.7 ± 2.8
SDSSJ084455.58+004718.15	0.1551	9.8 ± 0.2	-9.8 ± 0.4	12.2 ± 1.4
SDSSJ085829.88+022616.04	0.1097	9.4 ± 0.2	-9.6 ± 0.4	21.3 ± 0.9
SDSSJ090519.01+084933.70	0.3856	9.7 ± 0.3	-10.6 ± 1.0	42.6 ± 2.7
SDSSJ090519.61+084932.22	0.4545	9.6 ± 0.3	-8.9 ± 0.5	...
SSGAL090519.72+084914.02	0.1499	37.8 ± 2.0
SDSSJ091845.10+060202.93	0.1849	10.4 ± 0.2	-11.2 ± 0.8	< 0.3
SDSSJ093252.25+073731.59	0.3876	9.9 ± 0.3	-10.0 ± 1.1	30.9 ± 2.2
SDSSJ093537.25+112410.66	0.2808	9.7 ± 0.2	-9.8 ± 0.4	17.7 ± 1.2
SDSSJ100810.61+014446.17	0.2173	10.5 ± 0.2	-9.8 ± 0.3	14.6 ± 0.6
SDSSJ100906.91+023557.81	0.2523	10.5 ± 0.2	-10.7 ± 0.6	< 0.6
SDSSJ102220.71+013143.50	0.1369	10.7 ± 0.2	-11.5 ± 0.9	< 0.4
SDSSJ103605.26+015654.88	0.3571	10.6 ± 0.2	-9.8 ± 0.3	17.5 ± 1.0
SDSSJ103836.38+095143.68	0.1742	9.1 ± 0.2	-9.6 ± 0.3	18.4 ± 1.2
SDSSJ112016.63+093317.94	0.4933	10.6 ± 0.2	-10.1 ± 0.3	...
SDSSJ113756.76+085022.38	0.3356	9.9 ± 0.2	-9.8 ± 0.5	49.0 ± 2.1
SDSSJ114144.83+080554.09	0.2290	9.9 ± 0.2	-9.6 ± 0.3	18.5 ± 1.0
SDSSJ114145.14+080605.27	0.3583	10.2 ± 0.2	-10.0 ± 0.3	31.9 ± 4.6
SDSSJ120931.61+004546.23	0.2533	9.8 ± 0.2	-10.4 ± 0.6	< 1.1
SDSSJ122115.84-020259.37	0.0934	8.2 ± 0.2	-9.3 ± 0.3	...
SDSSJ125737.93+144802.20	0.4648
SDSSJ130555.49+014928.62	0.2258	10.2 ± 0.2	-10.1 ± 0.5	9.1 ± 0.5
SDSSJ130557.05+014922.34	0.1747	10.9 ± 0.2	-11.7 ± 0.8	< 0.4
SDSSJ132757.22+101136.02	0.2557	9.3 ± 0.2	-10.0 ± 0.9	43.5 ± 2.7
SDSSJ132831.54+075943.00	0.3323	10.4 ± 0.2	-10.0 ± 0.3	14.3 ± 1.2
SDSSJ132832.74+075952.56	0.2358	9.8 ± 0.2	-9.6 ± 0.5	36.0 ± 0.8
SDSSJ133905.86+002225.36	0.1438	10.6 ± 0.2	-11.4 ± 0.8	< 0.3
SDSSJ140618.34+130143.61	0.1748	10.4 ± 0.2	-10.3 ± 0.5	12.5 ± 0.4
SDSSJ140619.94+130105.23	0.2220	9.6 ± 0.2	-9.6 ± 0.3	26.8 ± 2.2
SDSSJ142600.05-001818.12	0.1382	11.3 ± 0.1	-11.8 ± 0.8	0.3 ± 0.1
SDSSJ143216.97+095522.23	0.3293	10.1 ± 0.2	-10.3 ± 0.5	39.5 ± 1.0
SDSSJ150339.62+064235.04	0.2333	9.3 ± 0.2	-9.8 ± 0.6	20.1 ± 1.2
SDSSJ150340.15+064308.11	0.1809	9.6 ± 0.2	-11.4 ± 0.8	< 3.8
SDSSJ151228.25-011216.09	0.1284	9.2 ± 0.1	-9.5 ± 0.3	13.9 ± 0.6
SDSSJ153112.77+091119.72	0.3265	9.8 ± 0.2	-9.8 ± 0.4	16.6 ± 1.5
SDSSJ153113.01+091127.02	0.2659	9.8 ± 0.2	-10.3 ± 0.5	10.3 ± 1.8
SDSSJ153715.67+023056.39	0.2151	9.5 ± 0.2	-9.5 ± 0.8	48.3 ± 1.6
SDSSJ155336.77+053438.23	0.3227	10.2 ± 0.1	-9.8 ± 0.3	< 15.2
SDSSJ155556.54-003615.58	0.3006	9.7 ± 0.4	-10.1 ± 0.8	34.4 ± 3.0
SDSSJ160749.54-002228.42	0.3985	10.6 ± 0.2	-10.1 ± 0.4	26.6 ± 2.0
SDSSJ160906.36+071330.66	0.2075	10.4 ± 0.2	-10.3 ± 0.5	14.6 ± 0.7
SDSSJ204303.53-010139.05	0.2356	9.9 ± 0.2	-9.2 ± 0.9	55.8 ± 0.7
SDSSJ204304.34-010137.91	0.1329	9.2 ± 0.2	-10.9 ± 0.9	< 0.8
SDSSJ210230.86+094121.06	0.3565	10.1 ± 0.3	-10.1 ± 0.5	29.7 ± 2.1
SDSSJ212938.98-063758.80	0.2782	9.7 ± 0.2	-10.1 ± 0.5	39.2 ± 2.2
SDSSJ221126.42+124459.93	0.4872	10.3 ± 0.3	-10.7 ± 0.9	...
SDSSJ221526.04+011353.78	0.3203	10.2 ± 0.2	-10.0 ± 0.5	27.3 ± 1.3
SDSSJ221526.88+011347.20	0.1952	9.1 ± 0.3	-9.5 ± 0.7	< 4.4
SDSSJ222849.01-005640.04	0.2410	10.0 ± 0.2	-10.3 ± 0.5	7.3 ± 2.3
SDSSJ223246.44+134655.34	0.3221	10.6 ± 0.2	-10.0 ± 0.4	16.4 ± 0.9
SDSSJ223316.34+133315.37	0.2138	9.9 ± 0.2	-9.6 ± 0.2	19.8 ± 1.0
SDSSJ223359.74-003320.83	0.1162	9.1 ± 0.2	-10.0 ± 0.6	27.6 ± 1.7
SDSSJ224704.01-081601.00	0.4270	10.8 ± 0.2	-10.3 ± 0.3	12.8 ± 1.5
SDSSJ230225.06-082156.65	0.3618	10.4 ± 0.2	-10.3 ± 0.4	66.0 ± 1.5
SDSSJ230225.17-082159.07	0.2146	8.4 ± 0.3	-8.7 ± 0.3	142.9 ± 4.3
SDSSJ230845.53-091445.97	0.2147	10.0 ± 0.2	-11.0 ± 0.9	< 0.6
SDSSJ232812.79-090603.73	0.1148	9.2 ± 0.1	-9.5 ± 0.6	28.4 ± 1.3
SDSSJ234949.42+003542.34	0.2778	10.1 ± 0.2	-10.3 ± 0.5	12.5 ± 1.2
"Group" Galaxies				
SDSSJ003339.66-005518.36	0.1760	10.1 ± 0.2	-11.7 ± 0.9	< 1.8
SDSSJ003341.47-005522.79	0.1758	8.9 ± 0.2	-9.5 ± 0.5	33.9 ± 4.0